A Bias-Flip Rectifier With Duty-Cycle-Based MPPT for Piezoelectric Energy Harvesting

Yue, Xinling; Javvaji, Sundeep; Tang, Zhong; Makinwa, Kofi A.A.; Du, Sijun

DOI
10.1109/JSSC.2023.3313733

Publication date
2024

Document Version
Final published version

Published in
IEEE Journal of Solid-State Circuits

Citation (APA)
Yue, X., Javvaji, S., Tang, Z., Makinwa, K. A. A., & Du, S. (2024). A Bias-Flip Rectifier With Duty-Cycle-Based MPPT for Piezoelectric Energy Harvesting. *IEEE Journal of Solid-State Circuits*, *59*(6), 1771-1781. https://doi.org/10.1109/JSSC.2023.3313733

A Bias-Flip Rectifier With Duty-Cycle-Based MPPT for Piezoelectric Energy Harvesting

Xinling Yue, *Graduate Student Member, IEEE*, Sundeep Javvaji, *Graduate Student Member, IEEE*, Zhong Tang, *Member, IEEE*, Kofi A. A. Makinwa, *Fellow, IEEE*, and Sijun Du, *Senior Member, IEEE*

***Abstract*— Bias-flip rectifiers are commonly employed for piezoelectric energy harvesting (PEH). This article proposes a synchronized switch harvesting on an inductor (SSHI) rectifier with a duty-cycle-based (DCB) maximum power point tracking (MPPT) algorithm. The proposed DCB MPPT algorithm is based on the mathematically derived relation between the MPPT efficiency and the duty cycle of the bridge rectifier. The resulting equation shows that the MPPT efficiency only depends on the rectifier duty cycle, and is independent of any other system variables, such as voltage bias-flipping efficiency, the open-circuit voltage from the harvester, vibration frequency, etc. As a result, MPPT can be achieved by regulating the duty cycle, simplifying circuit implementation, and achieving self-regulating and continuous MPPT. This design was fabricated in a 180-nm BCD process. The measured results show 98% peak MPPT efficiency and up to 738% output power enhancement.**

***Index Terms*— Bias-flip rectifier, duty-cycle-based (DCB), energy harvesting, maximum power point tracking (MPPT), piezoelectric energy harvester, synchronized switch harvesting on inductor (SSHI).**

I. INTRODUCTION

WITH the proliferation of the Internet of Things (IoT), there has been a growing focus on wireless sensor networks as a fundamental component of IoT deployments. As the need arises to power low-power devices efficiently and sustainably, energy harvesting systems have attracted considerable interest in both industry and academia. In this context, piezoelectric energy harvesting (PEH) has emerged as a particularly promising solution due to its inherent advantage of high power density. By harnessing the conversion of vibration energy into electrical energy, PEH offers a viable alternative to traditional bulky batteries in IoT applications, thereby addressing the limitations of limited battery life and frequent replacements [1], [2], [3], [4], [5], [6].

Rectifiers are essential in PEH systems to convert the ac output from piezoelectric transducers (PTs) into usable dc power. The full bridge rectifier (FBR) is the simplest and most commonly employed rectifier configuration for this purpose. It consists of four diodes arranged in a bridge configuration, allowing it to efficiently rectify the ac signal and generate a unidirectional dc output. The FBR's simplicity and widespread adoption make it a popular choice in PEH applications. However, passive FBRs have limited output power efficiency since the PT voltage relies solely on its generated charge for synchronous voltage flipping. To enhance energy extraction ability from PTs, active synchronized bias-flip rectifiers have gained popularity due to their enhanced performance [7], [8], [9], [10], [11]. Among them, the synchronized switch harvesting on inductor (SSHI) rectifier employs an inductor to create an RLC loop, effectively enhancing the output power efficiency [1], [12], [13], [14], [15], [16].

The output power derived from an SSHI rectifier is intricately tied to the inherent characteristics of the piezoelectric material, the properties of the excitation source, and the rectifier's flipping efficiency. Importantly, even though these parameters are known and constant initially, the output power will still vary, and it exhibits fluctuations in tandem with changes in the rectified voltage. As the rectified voltage transitions from low to high levels, the output power experiences an ascending trend followed by a decline. Within this range, a distinctive peak power value emerges, signifying an optimal power output point. Additionally, it is important to note that modifications to the excitation source or adjustments in the flipping efficiency lead to dynamic variations in the position of this peak power point. To determine this maximum power point (MPP), a maximum power point tracking (MPPT) technique is required. The conventional MPPT techniques used in energy harvesting systems are fractional open circuit voltage (FOCV) [5], [17], [18], [19] and perturb and observe (P&O) [14], [20], [21], [22].

Fig. 1(a) illustrates the FOCV MPPT technique consisting of an open circuit voltage (V_{OC}) sampler, an MPPT monitor, an ac–dc rectifier and a buck-boost dc–dc converter. In weakly coupled conditions, the PT can be modeled as an ac source I_P in parallel with a capacitor C_P. The rectified capacitor is denoted as C_{REC}, and the storage capacitor is denoted as C_S. The FOCV technique periodically measures the PT's open circuit voltage (V_{OC}) and regulates the rectified voltage (V_{REC}) to the optimal voltage V_{MPP}, corresponding to the MPP shown on the right side of Fig. 1(a). The optimal rectified voltage corresponds to the MPP, denoted as V_{MPP}, which can be expressed by $V_{\mathrm{MPP}} = V_{\mathrm{OC}}/(1-\eta_F)$ [23]. It is decided by the open circuit voltage V_{OC} and flipping efficiency η_F,

---

Manuscript received 7 July 2023; revised 18 August 2023; accepted 2 September 2023. Date of publication 2 October 2023; date of current version 29 May 2024. This article was approved by Associate Editor Pui-In Mak. *(Corresponding author: Sijun Du.)*

Xinling Yue, Sundeep Javvaji, Kofi A. A. Makinwa, and Sijun Du are with the Department of Microelectronics, Delft University of Technology, 2628CD Delft, The Netherlands (e-mail: sijun.du@tudelft.nl).

Zhong Tang is with the Department of Microelectronics, Delft University of Technology, 2628CD Delft, The Netherlands, and also with Vango Technologies Inc., Hangzhou 310053, China.

Color versions of one or more figures in this article are available at https://doi.org/10.1109/JSSC.2023.3313733.

Digital Object Identifier 10.1109/JSSC.2023.3313733

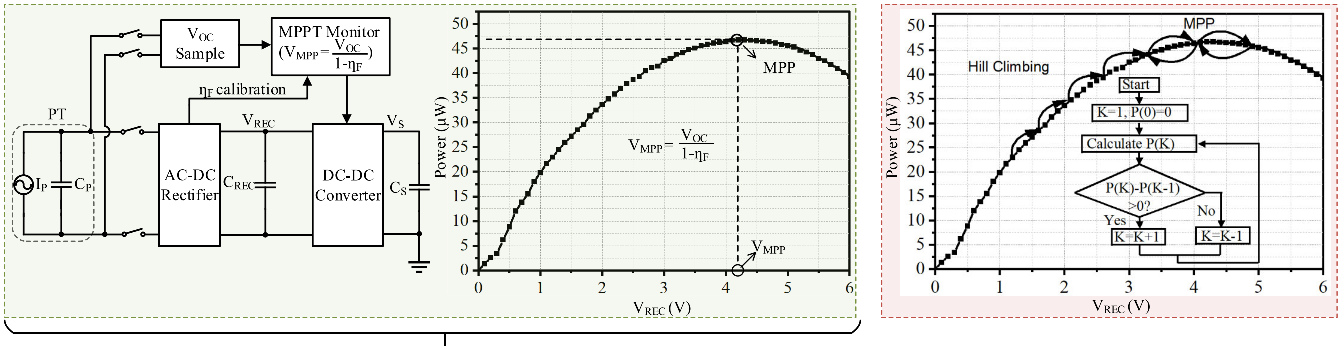

(a) (b)

Fig. 1. Two conventional MPPT techniques: FOCV and P&O.

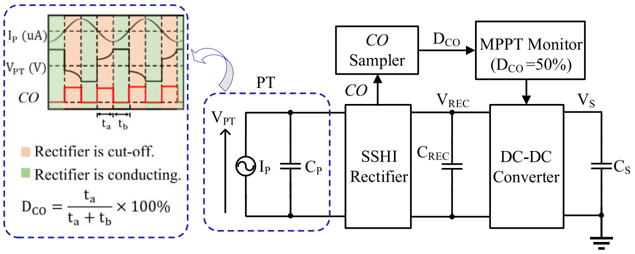

Fig. 2. Simplified diagram of the proposed DCB MPPT technique.

where the flipping efficiency (η_F) is defined as the voltage after being flipped by the active bias-flip rectifier divided by the voltage before flipping. Higher flipping efficiency directly corresponds to increased output power achievable through a bias-flip rectifier. The above V_{MPP} calculation shows some limitations. Periodically disconnecting the PT from the rectifier to measure V_{OC} results in wasted energy, while the inherent delay in sensing V_{OC} variations reduces overall tracking efficiency. Additionally, a calibration step is often required to determine V_{MPP} due to its dependence on the PT voltage flip efficiency (η_F) of the bias-flip rectifier. System parameters such as inductance, parasitic resistors, and capacitors can easily affect η_F, necessitating the update of V_{MPP}. Consequently, accurately tracking V_{MPP} becomes more challenging.

Fig. 1(b) shows another MPPT algorithm, P&O, which adjusts the rectified output power step-wise toward the MPP [14]. If the measured power in the current step is higher than in the previous step, it continues to climb toward the MPP. In a steady state, it keeps searching back and forth around the MPP, thus establishing robust and continuous MPPT. This method is independent of the energy harvester's characteristics and achieves continuous tracking. However, accurately sensing the rectified output power in small increments often requires complex circuit implementation and may result in power-hungry hardware.

This article proposes a duty-cycle-based (DCB) MPPT technique, which is validated using an SSHI rectifier as shown in Fig. 2. The system comprises four main blocks: an SSHI rectifier, a dc–dc buck–boost converter, a cut-off (CO) sampler, and an MPPT monitor. During the ac energy extraction from the PT, the rectifier switches periodically between conducting and cut-off modes, generating a cut-off signal, CO. This signal is "high" when the rectifier is in the cut-off state and "low"'s when it is conducting, as shown on the left side of the figure. The duty cycle of the cut-off signal, denoted as D_{CO}, represents the rectifier's cut-off time.

Unlike the FOCV method, which samples the open circuit voltage and the P&O method, which measures the rectified output power, a mathematical analysis shows that the MPP solely corresponds to a CO duty cycle of 50%. If $D_{\mathrm{CO}} < 50\%$, indicating that the MPP has not been reached, the dc–dc converter is disabled and the voltage V_{REC} continues to increase as it is charged by the PT. Conversely, if $D_{\mathrm{CO}} \geq 50\%$, signifying that the MPP has been reached, the dc–dc converter is enabled to decrease the duty cycle by transferring some energy from C_{REC} to C_S. The proposed DCB MPPT algorithm offers several advantages over conventional FOCV and P&O techniques:

1) it is independent of open-circuit voltage, V_{OC}, and flipping efficiency, η_F, eliminating the need for calibration;
2) the PT remains continuously connected to the rectifier, resulting in no wasted energy;
3) it achieves continuous and automatic MPPT;
4) it features simplified circuit implementations;
5) it has low power consumption of only 307 nW;
6) it demonstrates strong robustness to duty cycle errors.

II. THEORETICAL ANALYSIS OF THE PROPOSED DCB MPPT TECHNIQUE

The proposed DCB MPPT algorithm exploits the relationship between the MPPT efficiency, η_{MPPT}, and the duty cycle of the rectifier CO signal, D_{CO} [7].

When a weakly coupled PT is vibrating at its natural frequency, the PT can be modeled as a current source, I_P, in parallel with a capacitor, C_P. The current source, I_P, can be expressed as

$$I_P = I_0 \sin(\omega t) \tag{1}$$

where I_0 is the amplitude and ω is the excitation frequency.

The total generated charge, Q_{total} from the PT, in a half vibration period, $(T/2)$, can be expressed by

$$Q_{\mathrm{total}} = \int_0^{\frac{T}{2}} I_0 \sin(\omega t) dt = \frac{2I_0}{\omega}. \tag{2}$$

The open circuit zero-to-peak voltage amplitude, V_{OC}, can be expressed as

$$V_{\mathrm{OC}} = \frac{1}{2}\frac{Q_{\mathrm{total}}}{C_P} = \frac{I_0}{\omega C_P}. \tag{3}$$

Assuming that the diode voltage drop, V_D, of the bridge rectifier is zero, and noting η_F as the voltage flipping efficiency of the bias-flip rectifier, the charge wasted in a half vibration period is

$$Q_{\mathrm{Waste}} = C_P V_{\mathrm{REC}}(1-\eta_F). \tag{4}$$

The remaining charge will flow into the output capacitor C_{REC}. This amount of charge, Q_{SSH}, can be expressed as

$$Q_{\mathrm{SSH}} = Q_{\mathrm{total}} - Q_{\mathrm{Wasted}} = Q_{\mathrm{total}} - C_P V_{\mathrm{REC}}(1-\eta_F). \tag{5}$$

By applying (2) and (3), the Q_{SSH} can also be written as

$$Q_{\mathrm{SSH}} = C_P(2V_{\mathrm{OC}} - V_{\mathrm{REC}}(1-\eta_F)). \tag{6}$$

The equation above shows the extracted charge in a half-vibration period, $T/2$. Thus, the extracted power, P_{SSH}, for the active synchronized switch rectifier can be approximately written as

$$P_{\mathrm{SSH}} = 2 f_P C_P V_{\mathrm{REC}}(2V_{\mathrm{OC}} - V_{\mathrm{REC}}(1-\eta_F)). \tag{7}$$

When setting its derivative to V_{REC} at 0, it can be found that the peak power at the MPP, P_{MPP}, is obtained as follows:

$$P_{\mathrm{MPP}} = \frac{2C_P f_P V_{\mathrm{OC}}^2}{1-\eta_F}. \tag{8}$$

By setting η_{MPPT} as the MPPT efficiency, it is the ratio between actual output power, given by (7), and the peak power at MPP, given by (8). This is expressed as

$$\eta_{\mathrm{MPPT}} = \frac{P_{\mathrm{SSH}}}{P_{\mathrm{MPP}}}. \tag{9}$$

Substituting (7) and (8) into (9), this can be expressed as

$$\eta_{\mathrm{MPPT}} = \frac{V_{\mathrm{REC}} \times [2V_{\mathrm{OC}} - V_{\mathrm{REC}}(1-\eta_F)](1-\eta_F)}{V_{\mathrm{OC}}^2}. \tag{10}$$

Substituting (3) into (10), (10) can be rewritten as

$$\eta_{\mathrm{MPPT}} = \frac{V_{\mathrm{REC}} \times \left[2\frac{I_0}{\omega C_P} - V_{\mathrm{REC}} \times (1-\eta_F)\right](1-\eta_F)}{\left[\frac{I_0}{\omega C_P}\right]^2}. \tag{11}$$

(11) shows the MPPT efficiency of the rectifier for a given vibration amplitude, I_0 (or V_{OC}), and voltage bias-flip efficiency, η_F. We will then replace these two variables with the rectifier cut-off duty cycle.

We define D_{CO} as the cut-off duty cycle of the rectifier as shown on the left of Fig. 2. The generated charge is wasted during the cut-off period because all the charge generated in this period is used to build up the PT voltage. We define that t_{off} represents the cut-off time, and t_{on} denotes the conducting time of the rectifier in a half-vibration period. Assuming the bias-flip operation happens exactly at the zero-crossing moment of the current source I_P, the total wasted charge Q_{waste} in the cut-off time can be written as

$$Q_{\mathrm{waste}} = \int_0^{t_{\mathrm{off}}} I_0 \sin \omega t dt. \tag{12}$$

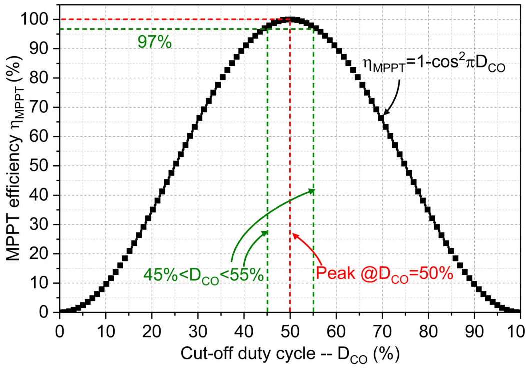

Fig. 3. Equation plotting of the MPPT efficiency in function of the cut-off duty cycle.

Considering that the duty cycle $D_{\mathrm{CO}} = t_{\mathrm{off}}/(t_{\mathrm{on}} + t_{\mathrm{off}})$ and the half cycle is expressed by $t_{\mathrm{on}} + t_{\mathrm{off}} = T/2$, t_{off} can be written as

$$t_{\mathrm{off}} = D_{\mathrm{CO}} * (t_{\mathrm{on}} + t_{\mathrm{off}}) = \frac{D_{\mathrm{CO}}T}{2}. \tag{13}$$

Substituting (13) into (12), (12) can be written as

$$\begin{aligned} Q_{\mathrm{waste}} &= \int_0^{t_{\mathrm{off}}} I_0 \sin \omega t dt \\ &= \int_0^{\frac{D_{\mathrm{CO}}T}{2}} I_0 \sin \omega t dt \\ &= \frac{I_0}{\omega}(1 - \cos(\pi D_{\mathrm{CO}})). \end{aligned} \tag{14}$$

While (4) gives the wasted charge in a half period from the perspective of the rectifier output, (14) gives the same wasted charge from the perspective of the input. Combining (4) and (14), we have

$$V_{\mathrm{REC}}(1-\eta_F) = \frac{I_0(1-\cos(\pi D_{\mathrm{CO}}))}{\omega C_P}. \tag{15}$$

Substituting (15) into (11), the η_{MPPT} can be rewritten as

$$\begin{aligned} \eta_{\mathrm{MPPT}} &= \frac{\frac{2\frac{I_0}{\omega}(1-\cos(\pi D_{\mathrm{CO}}))\times I_0}{\omega} - \left[\frac{I_0}{\omega}(1-\cos(\pi D_{\mathrm{CO}}))\right]^2}{\left(\frac{I_0}{\omega}\right)^2} \\ &= 2 \times (1-\cos(\pi D_{\mathrm{CO}})) - [1-\cos(\pi D_{\mathrm{CO}})]^2. \end{aligned} \tag{16}$$

After simplification, (16) can be expressed as

$$\eta_{\mathrm{MPPT}}(D_{\mathrm{CO}}) = 1 - \cos^2(\pi D_{\mathrm{CO}}). \tag{17}$$

By setting the derivative of (17) at 0, the MPPT efficiency can theoretically achieve 100% when $D_{\mathrm{CO}} = 50\%$. This can also be seen by plotting v_{MPP} versus D_{CO} shown in Fig. 3. This relation between the MPPT efficiency and the rectifier cut-off duty cycle provides a clean and simple way to achieve MPPT in PEH. Different from conventional FOCV and P&O algorithms, this DCB algorithm only needs to regulate D_{CO} at 50%, without considering the vibration amplitude V_{OC} or voltage flip efficiency η_F. Moreover, due to the squared cosine relationship, the proposed DCB algorithm exhibits robustness to sensing errors in D_{CO}. For instance, with a ±5% error in D_{CO}, the MPPT efficiency η_{MPPT} remains above 97%, as illustrated in Fig. 3.

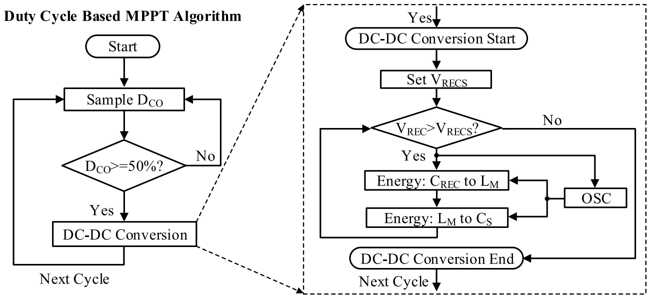

Fig. 4. Working flow of the proposed DCB MPPT system.

III. System Architecture

The flowchart of the proposed DCB MPPT technique is shown in Fig. 4. It begins by sampling the duty cycle, D_{CO}. It is sampled in every CO period by measuring its on and off pulse widths. If the measured $D_{\mathrm{CO}} < 50\%$, energy harvested by the PT charges the rectifier output capacitor C_{REC}, thus increasing its voltage, V_{REC}, toward the MPP, resulting in an increasing D_{CO}. Conversely, if the measured $D_{\mathrm{CO}} \geq 50\%$, this means that V_{REC} is equal to or exceeds the V_{MPP}. Consequently, some of the energy stored in C_{REC} is transferred to the storage capacitor C_S via a dc–dc buck-boost converter in order to maintain V_{REC} around V_{MPP} by regulating D_{CO} to around 50%. The dc–dc converter operation is shown on the right of Fig. 4. Initially, a slightly lower voltage level, denoted as V_{RECS}, is set as the lower threshold of the hysteresis window for V_{REC}. The energy conversion process involves two steps: first, dumping the energy from the rectified capacitor, C_{REC}, to the sharing inductor, L_M; and then it is subsequently transferred from L_M to the storage capacitor C_S. The buck–boost conversion operates for multiple cycles until $V_{\mathrm{REC}} < V_{\mathrm{RECS}}$. To prevent a large current flow through the inductor, the energy transfer timing is clocked by an on-chip oscillator (OSC). This flow repeats until the next time when D_{CO} exceeds 50%, thereby achieving MPPT.

The proposed system architecture comprises an SSHI rectifier with its dedicated control block, a buck–boost dc–dc converter, and an MPPT controller, as shown in Fig. 5. The SSHI rectifier comprises an FBR, an active diode, and an off-chip inductor, L_M that is shared with the buck–boost dc–dc converter. When there is a need to flip the voltage across the PT (V_{PT}), the bridge rectifier switches from the conducting mode to the cut-off mode; this transition causes the CO signal to have a rising edge, which is utilized to generate an SSHI flipping pulse through the control logic I and pulse generation block. The CO signal is first processed by control logic I block to generate a stable synchronized signal, SYN. During the dc–dc conversion period, the SYN is affected by the MPPT ending signal, referred to as END. When the END signal is high, the SYN remains low, which disables the pulse generation block. The generation and explanation of the END signal are presented, which will be explained in Section IV. When the SYN signal experiences a rising edge, the pulse generation block generates a pulse. Following the level shifters, the resulting pulse, denoted as Φ, briefly connects L_M across the PT, initiating a closed RLC loop to flip the PT voltage, V_{PT}. The MAX block is responsible for selecting a higher voltage to serve as the power supply for the level shifters.

In addition to its usage in the control of the SSHI rectifier, the CO signal is also transmitted to the MPPT controller, as illustrated on the right side of Fig. 5. The MPPT controller is triggered by the falling edge of CO to avoid the conflict between the two blocks. The MPPT controller consists of seven main blocks: a duty cycle assessment block, two control logic blocks, a V_{RECS} range set up block, a zero-crossing detection (ZCD) block, an OSC and level shifters.

The duty cycle D_{CO} is measured by a duty cycle assessment block and fed to the control logic II. If D_{CO} exceeds 50%, a COM signal is generated through the control logic II and sent to a V_{RECS} range set-up block in Fig. 5. To prevent V_{REC} from dropping excessively, a hysteresis window is established with a lower voltage threshold, V_{RECS}, which is a fraction of the initial rectified voltage V_{REC}. The upper hysteresis threshold is automatically set to V_{MPP} based on the condition $D_{\mathrm{CO}} = 50\%$, eliminating the need for an explicit voltage threshold. The V_{RECS} range set-up block, implemented as a capacitor array, will be described in the circuit implementation section.

The rectified voltage V_{REC} and sampled low hysteresis voltage V_{RECS} are compared to generate a signal, COMH, which is then fed to the control logic III block. This block combines the outputs of an on-chip OSC and a ZCD block. The ZCD block is employed to prevent the reverse current while transferring the energy from L_M to C_S. After passing through the level shifters, the switching signals S_{PD} and S_{PC} are used to control the buck–boost dc–dc converter. The buck–boost converter uses the shared inductor, L_M to transfer dc energy from C_{REC} to C_S in multiple steps, following the same process as introduced in the flowchart of the dc–dc conversion process in Fig. 4. Therefore, the MPPT is achieved by regulating the duty cycle, D_{CO} at 50%.

IV. Circuit Implementation

Fig. 6 illustrates the MPPT controller block. Every CO signal is fed into the duty cycle sampler block for duty cycle assessment. In this block, the duty cycle, D_{CO}, is sensed using two equal on-chip capacitors, C_{RGL} and C_{RGR} as shown in the top-left of Fig. 6. When CO is high, C_{RGL} is charged by an on-chip current source, I_{RG}, to V_H; while C_{RGR} is charged to V_L when CO is low. To cope with a wide range of PT vibration frequency, which is the half of CO frequency, C_{RGL} and C_{RGR} can be adjusted in eight steps between 5.4 and 32.4 pF. The resulting voltages V_H and V_L are compared to generate the PO signal, which indicates the polarity of D_{CO} around the 50% target. When $D_{\mathrm{CO}} \geq 50\%$, PO stays low; otherwise, a pulse is generated. The C_{RGL} and C_{RGR} are reset by a short pulse, S_{CV}, at the end of each CO period. When PO stays low, meaning that D_{CO} exceeds 50% (or V_{REC} exceeds V_{MPP}), a dc–dc enable signal, COM, is generated to start the dc–dc conversion. The lower hysteresis threshold, V_{RECS}, is generated by a switched-capacitor voltage divider. In this design, V_{RECS} can be turned from $97\% \times V_{\mathrm{REC}}$ to $99.5\% \times V_{\mathrm{REC}}$, by tuning ex1, ex2, and ex3 to adjust the ripple of V_{REC} during dc–dc conversion. The rectified voltage V_{REC} and its low hysteresis

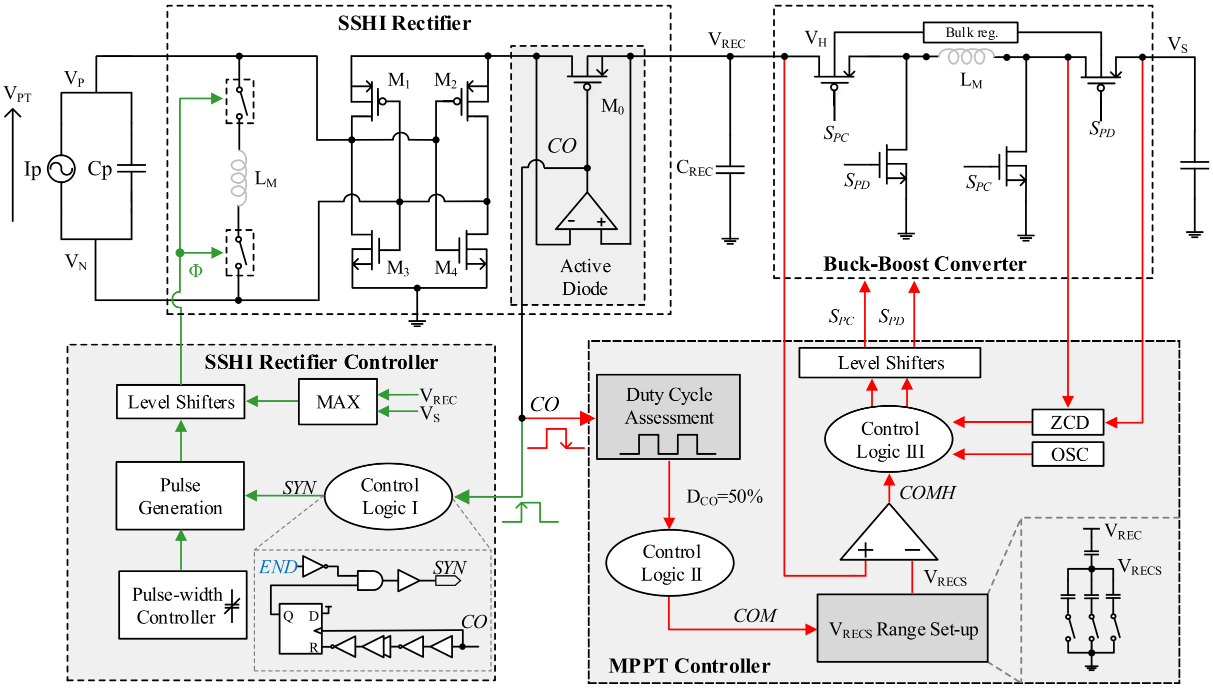

Fig. 5. System architecture of an SSHI rectifier with the proposed DCB MPPT technique.

voltage are compared to generate a COMH signal, which turns to high when $V_{\mathrm{REC}} < V_{\mathrm{RECS}}$. Control logic III generates the dc–dc conversion control signals, through the level shifters, to drive the switches in the dc–dc conversion loop, by combining COMH and other signals generated by the OSC and ZCD blocks. Further details about the circuitry of control logic III will be presented in the following.

The detailed circuit implementation of the control logic III block is shown in Fig. 7. It combines the output signals of OSC, ZCD, CO, and COMH together in order to generate two dc–dc conversion control signals, S_{PC} and S_{PD}. On the top of Fig. 7, the ZCD is to compare the voltages between the switch which connects the right end of the inductor L_M and storage capacitor C_S in order to prevent the reverse current flowing output of C_S. When the voltage of the left end of the switch is lower than the right point, a dc–dc conversion stopping signal, STD, will generate a rising edge. This process repeats in every energy dumping period between L_M and C_S. The MPPT ending signal, END, is affected by STD, COMH, and CO, indicating that the MPPT period is decided by the results of ZCD, dc–dc rectified low window voltage of MPPT, and cut-off duty cycle respectively. When the END generates a rising edge which means that dc-dc conversion in the current MPPT period has finished and will be restarted until the next MPPT comes.

The bottom of Fig. 7 shows how the dc–dc converter control signal, S_{PC}, S_{PD} are generated. Its ending time is mainly decided by the END signal and clocked by an OSC. Through the level shifters, the S_{PC} and S_{PD} are finally generated. The S_{PC} controls the time of dumping energy from the rectified capacitor C_{REC} to the inductor and S_{PD} is the time for the inductor to dump energy to the storage capacitor. The S_{PC} is shorter than S_{PD} and both of them are determined by the oscillator and a counter's signal, CNT_1, as shown in Fig. 7.

In the design of the DCB MPPT system, an on-chip constant-gm bias circuit is utilized to generate the required bias currents. This bias circuit is shown in Fig. 8. The purpose of the constant-gm bias circuit is to provide a stable bias current across process corners and variations. To achieve this, the bias resistor R_b is designed to be tunable, ranging from 1 to 5 M with 1 M steps. By adjusting the value of R_b, the bias current can be maintained at a desired level regardless of process variations. In addition, an auxiliary amplifier is employed in the bias circuit to enhance the power supply rejection ratio (PSRR). By incorporating the auxiliary amplifier, the bias circuit becomes less sensitive to power supply voltage fluctuations, thereby improving the stability of the generated bias currents.

V. MEASUREMENT RESULTS

The experimental setup and a chip micrograph are shown in Fig. 9. The proposed circuit was fabricated in a 180-nm BCD process with an active area of 0.47 mm^2. The chip contains seven main blocks, a tunable D_{CO} sampling block, a power supply selector, a dc–dc converter, level shifters, a bias current generation block, an SSHI rectifier, and a tunable V_{RECS} generation block. The chip was tested with a commercial PT (PEH-S128-H5FR-1107YB) excited at its resonance frequency of 230 Hz during the experiments.

Fig. 10 shows the measured waveform of V_S and V_{REC}. The system starts from the cold state with a vibration excitation level equivalent to $V_{\mathrm{OC}} = 1.5$ V. An inductor of $L_M = 27\ \mu$H is employed. In the beginning, V_{REC} increases steadily

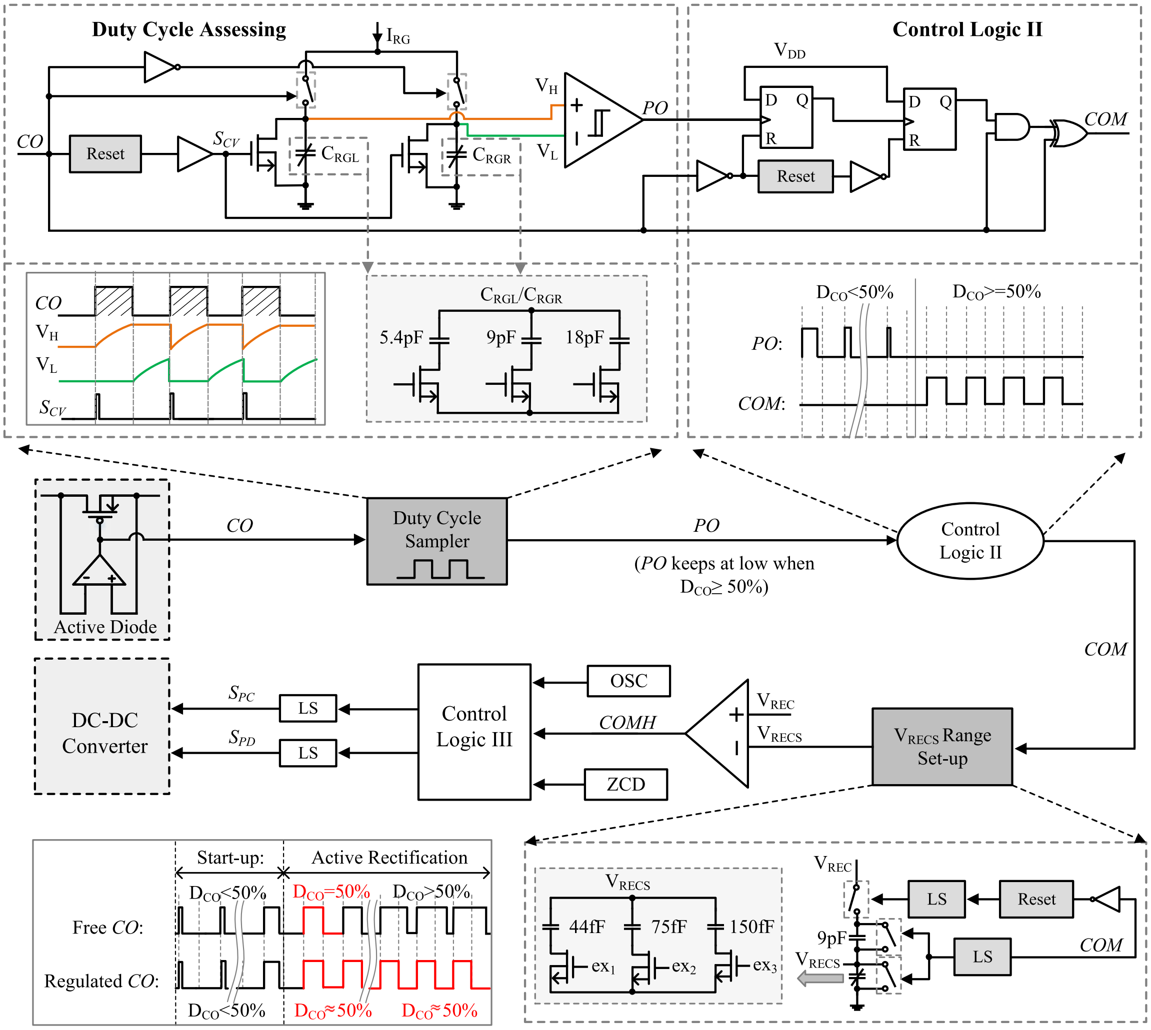

Fig. 6. Detailed circuit diagrams of the MPPT controller block.

because the initial duty cycle D_{CO} is less than 50% and the dc–dc converter is disabled. Once V_{REC} reaches the first optimal voltage according to MPP, V_{MPP1} (around 2.6 V), D_{CO} achieves 50%. The dc–dc converter is then enabled by the MPPT controller to regulate D_{CO} at 50% (or V_{REC} at 2.6 V) during the MPPT$_1$ period by transferring the extra harvested energy to V_S. This dc–dc conversion results in a rising V_S. To observe the tracking ability of the proposed MPPT technique on varying V_{OC}, the vibration excitation level is increased to $V_{\text{OC}} = 2$ V. As expected, V_{REC} increases to track the higher MPP due to the larger excitation. This is because D_{CO} becomes less than 50% once V_{OC} is increased, which makes the system regulating D_{CO} back to 50%. To achieve this, the dc–dc converter is disabled to let V_{REC} increase until D_{CO} reaches 50% again. This indicates that the proposed circuit can sense the vibration excitation variation by measuring D_{CO} in only a half vibration cycle after the variation occurs, and start to track the new MPP. Once D_{CO} reaches 50% again, which means V_{REC} achieves the new MPP, the dc–dc converter starts to operate to maintain V_{REC} at this new MPP by regulating D_{CO} at 50%. The new MPPT period at this higher excitation level is labeled MPPT$_2$.

The slight increasing slope of V_{MPP2} during the MPPT$_2$ period is because the voltage V_S replaces V_{REC} to power the bias-flip switches in the SSHI rectifier when $V_S > V_{\text{REC}}$. The MAX block in Fig. 5 selects a higher voltage for the power supply of the level shifters, which lowers the conducting resistance of the bias-flip switches. This slightly increases the voltage flipping efficiency and, consequently, the optimal rectified voltage V_{MPP} increases, as explained by the equation: $V_{\text{MPP}} = V_{\text{OC}}/(1 - \eta_F)$. These observations indicate that the proposed DCB MPPT algorithm can automatically track the MPP regardless of system and environmental parameters. The convergence time of MPPT is mainly affected by the capacitance of C_{REC}; the larger the C_{REC} is, the longer the convergence time is needed. The V_{REC} voltage ripple during MPPT is around 289 mV, which can be configured by adjusting the hysteresis window.

The zoomed-in V_{REC} during the MPPT$_2$ period is picked up in Fig. 11. The V_{REC} stabilizes at approximately 3.42 V. To prevent excessive voltage drop, V_{REC} is gradually reduced in multiple dc–dc conversion steps. Each dc–dc working period consists of two phases, controlled by signals S_{PC} and S_{PD}. These signals regulate the charging time from C_{REC} to L_M and

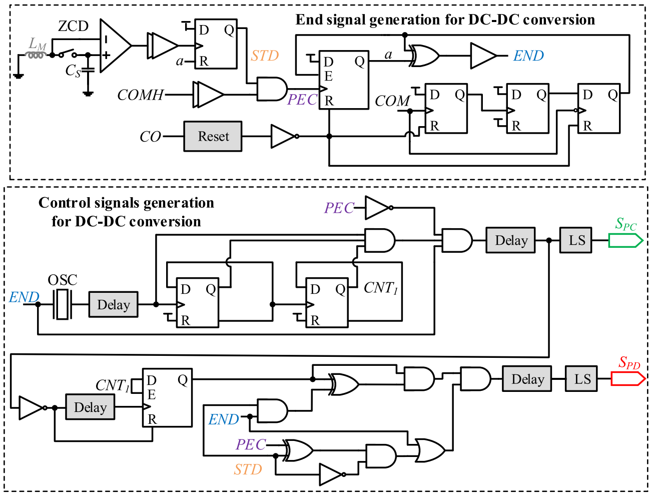

Fig. 7. Circuit diagram of the control logic III block.

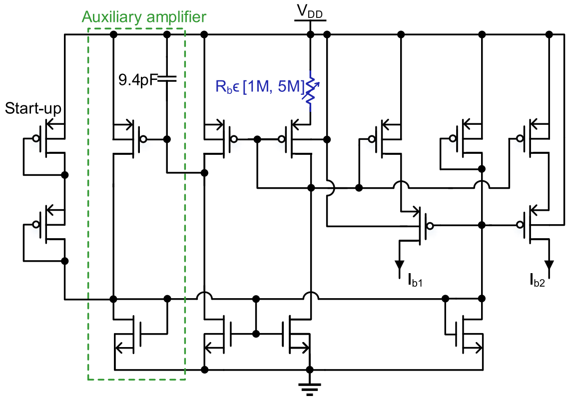

Fig. 8. Bias current generation for the system.

from L_M to C_S, respectively. Control logic III, illustrated in Fig. 7, generates the S_{PC} and S_{PD} signals. In the bottom part of Fig. 11, the duration of S_{PC} is shown to be approximate 1.4 μs. This timing control ensures the suitable charging of the different components within the dc–dc conversion process.

Fig. 12 presents the measured PT voltage, V_{PT}. The amplitude of V_{PT} aligns with V_{REC} depicted in Fig. 10. When V_{OC} is increased from 1.5 to 2 V, the MPPT process is reflected by the V_{PT} shown in the zoomed-in waveform at the bottom. In this specific measurement scenario, C_{REC} is 10 μF. It takes approximately 0.2 s for the system to achieve the new MPP after the V_{OC} change. Less time is needed if a smaller C_{REC} is used. The peak-to-peak value of V_{PT} is changed from 5.2 to 6.4 V due to increasing C_{REC}.

Fig. 13 shows the cut-off signal, CO. During the startup period, the duty cycle of CO, D_{CO}, is less than 50%. As D_{CO} approaches 50%, the MPP is getting closer. In the MPPT$_1$ period, the D_{CO} is around 49.98% and in MPPT$_2$, the D_{CO} is around 50.19%. Both values are very close to 50%. The top right sub-figure zooms in the waveforms of V_{PT} and CO. It demonstrates that when CO is high, the rectifier is in a cut-off state and V_{PT} gradually builds up. When CO switches to low, V_{PT} is clamped at V_{REC}, indicating the onset of the conducting state. Therefore, the 50% denotes the on/off time ratio of the rectifier, which is also reflected by the waveform of V_{PT}.

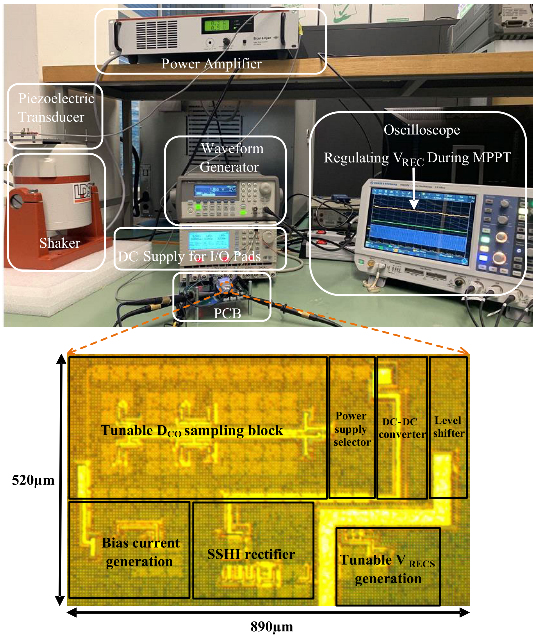

Fig. 9. Experimental setup in the Laboratory and chip microphoto.

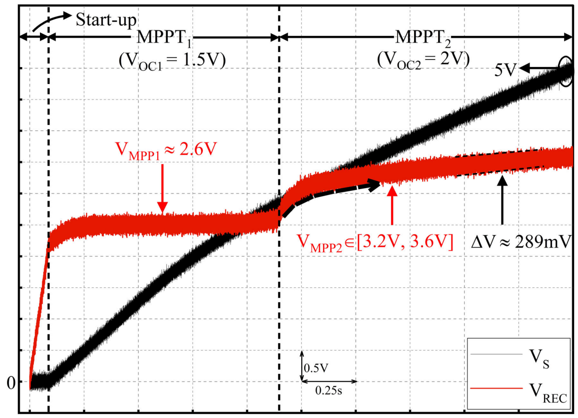

Fig. 10. Measured waveform of V_S and V_{REC} during the MPPT transient time with input 1.5 and 2-V V_{OC}.

Fig. 14 presents the measured output power of the SSHI rectifier as a function of D_{CO}. It can be observed that the output power varies with different duty cycles and reaches the peak at an optimal duty cycle. The measured peak power of the SSHI rectifier is 48.52% and 47.58% for $V_{\mathrm{OC}} = 1.5$ V and $V_{\mathrm{OC}} = 2$ V respectively, slightly lower than the theoretical value of 50%. The shift in the optimal duty cycle from 50% to a slightly lower value is primarily caused by the nonzero voltage drop of the active rectifier and the inaccuracy of the CO signal. Despite the actual duty cycle not being exactly 50%, this work still adopts 50% as the regulation target. By regulating D_{CO} at 50%, the measured MPPT efficiencies for the two measurement conditions are 99.9% and 99.7%, very close to the peaks at 48.52% and 47.58% duty cycle, respectively. This indicates that the DCB MPPT technique exhibits strong robustness to errors in the duty cycle (D_{CO}), consistent with the analysis shown in Fig. 3 based on the cosine-squared relationship. The measured output power values of the SSHI rectifier at $V_{\mathrm{OC}} = 1.5$ V and $V_{\mathrm{OC}} = 2$ V are 69.9 and 124.9 μW, respectively.

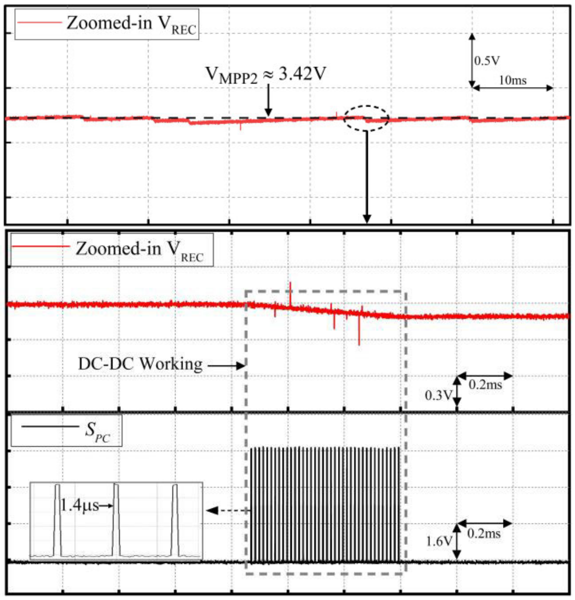

Fig. 11. Zoomed-in waveform of V_{REC} and S_{PC} of a dc–dc conversion moment during MPPT.

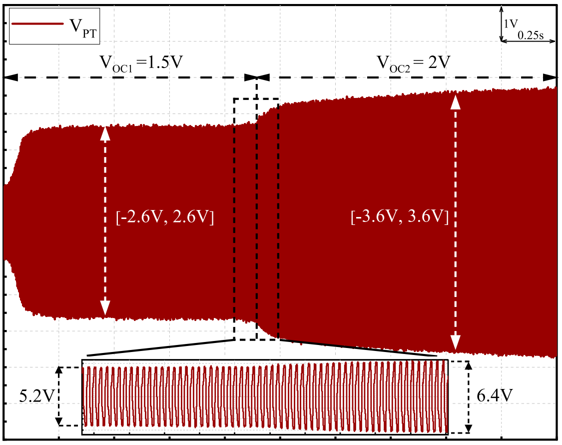

Fig. 12. Measured waveform of V_{PT} during the MPPT transient time with 1.5- and 2-V V_{OC} input.

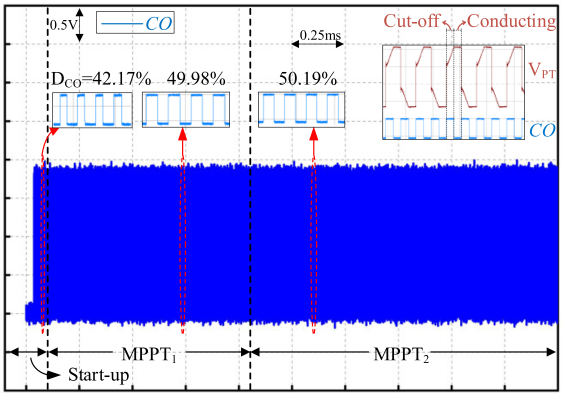

Fig. 13. Measured cut-off signal CO during the transient time.

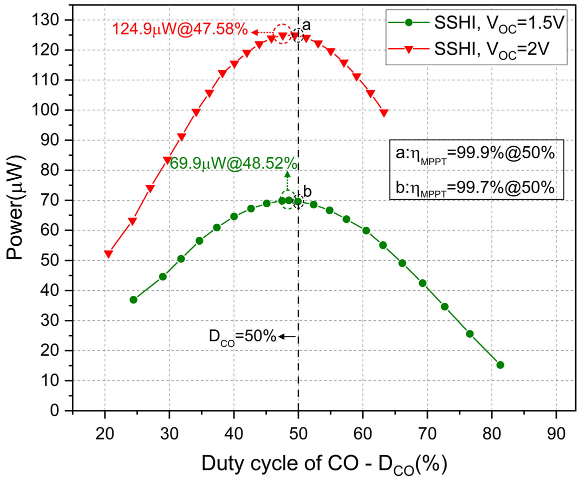

Fig. 14. Output power of an SSHI rectifier versus the duty cycle, D_{CO}.

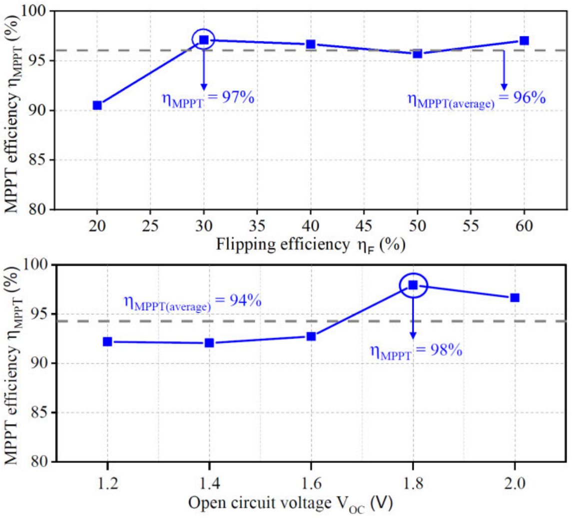

Fig. 15. MPPT efficiency versus η_F and V_{OC}.

In order to verify that the proposed DCB MPPT technique is independent of voltage flipping efficiency, η_F, and open-circuit voltage amplitude, V_{OC}, Fig. 15 shows the MPPT efficiency over different η_F and V_{OC} by changing the off-chip inductor and vibration excitation level. The range of flipping efficiency spans from 20% to 60% with a step size of 10%. The peak MPPT efficiency reaches 97% and the average value remains around 96% for high flipping efficiency values. In the second sub-figure, the V_{OC} is varied from 1.2 to 2 V with a step size of 0.2 V. The highest MPPT efficiency is achieved at 98% when $V_{OC} = 1$ V. These results demonstrate that the DCB MPPT technique is independent of varying flipping efficiency η_F and open circuit voltage V_{OC}, and it maintains a high tracking efficiency in large variation ranges of η_F and V_{OC}. Due to process limitations (maximum device breakdown voltage at 5 V), V_{OC} and η_F cannot be set too high, according to the relationship $V_{MPP} = V_{OC}/(1 - \eta_F)$, since they could push V_{MPP} above 5 V and the MPP cannot be achieved with the process. For measurements in a wider range of V_{OC} and η_F, a process with high-voltage devices, or off-chip high-voltage switches, can be used in future works.

Fig. 16 shows the true optimal D_{CO} in wide ranges of η_F and V_{OC}. To obtain the true optimal D_{CO} values, the MPPT block keeps disabled, and the system operates solely as an SSHI rectifier. In this way, the rectified output power can be

TABLE I

PERFORMANCE COMPARISON WITH PREVIOUS WORK

	JSSC'15 [17]	ISSCC'16 [5]	ISSCC'19 [18]	VLSI'19 [14]	ISSCC'20 [20]	ISSCC'22 [24]	**This work**
Technology	350 nm	350 nm	180 nm	130 nm	600 nm	65 nm	180 nm
Technique	Comparator based	P-SSHI	SPFCR	P-SSHI	PSECE	SECE	**SSHI**
Harvester Type	Mide-V21BL	Mide-V21/V22B	PPA1021	PPA1021/1011	PEH	TEG/PV/PEH	**PEH-1107YB**
C_P (nF)	11	26/20/9	22	20/100	24	24	**42**
Frequency (Hz)	100*	134.6-229.2	200	100-180	56	–	**230**
V_{OC}(V)	2	1.25	1.4	3	–	–	**1.2-2**
MPPT Technique	FOCV	FOCV	FOCV	P&O	P&O	FOCV	**DCB**
Continuous MPPT?	No	No	No	Yes	Yes	No	**Yes**
ADC/DAC/Sensor needed?	–	–	Yes	No	Yes	Yes	**No**
V_{OC} Sampling needed?	Yes	Yes	Yes	No	Yes	Yes	**No**
Peak MPPT Efficiency	99%	–	–	97%	94%	80%	**98%**
Chip area (mm^2)	5.5	1.3*	0.21	1.07	14	3.11	**0.47**
Quiescent Current (μA)	3	–	–	0.9	0.3	–	**0.17**
Flipping efficiency-η_F	–	89%/94%	89%	–	–	No	**82%**
P_{IC}/P_{FBR}	100%	440%	650%-930%	417%	328%	320%	**738%**

*: Estimated value. –: Not reported.

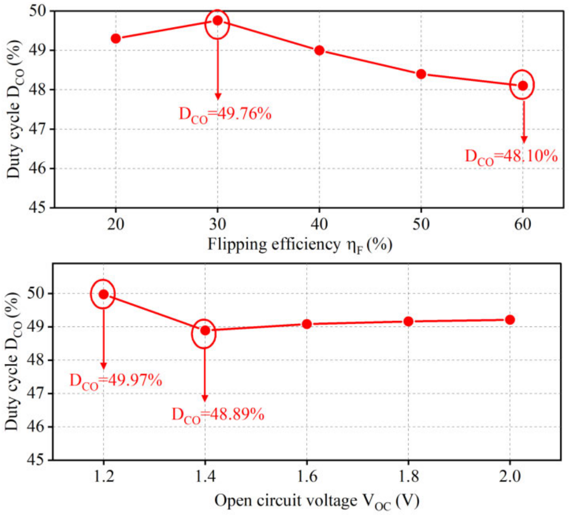

Fig. 16. True optimal duty cycle for different η_F and V_{OC}.

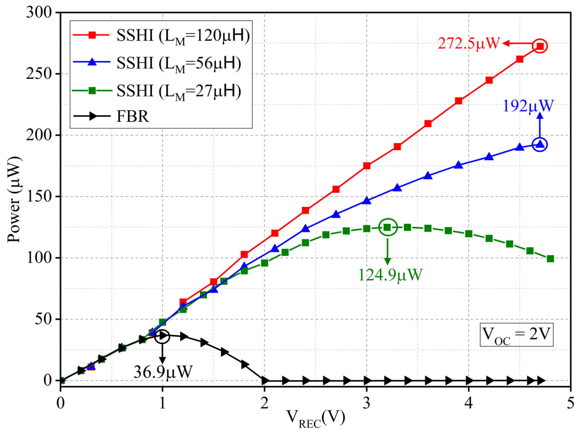

Fig. 17. Output power of FBR and SSHI rectifiers versus output voltage V_{REC} with 2-V V_{OC}.

measured in a range of V_{REC} to find the peak, and the true optimal D_{CO} can be calculated from the CO signal at the power peak. From the two subfigures, it can be seen that the true optimal D_{CO} values keep very close to 50% regardless of η_F and V_{OC}. The worst case D_{CO} values are 48.10% at $\eta_F = 60\%$ and 48.89% at $V_{OC} = 1.4$ V. However, this deviation has a minimal impact on the actual peak MPPT efficiency due to the robustness of the proposed MPPT algorithm against D_{CO} errors. Therefore, even when regulating the D_{CO} always at 50%, the peak MPPT efficiency can still be very high, demonstrating the effectiveness of the proposed MPPT algorithm and its ability to tolerate D_{CO} errors.

Fig. 17 shows the output power of the FBR and SSHI rectifier for different rectified voltage levels. The measurements are conducted with a fixed open circuit voltage amplitude $V_{OC} = 2$ V. The peak output power achieved by the FBR is 36.9 μW, with the corresponding V_{MPP} around 1 V. On the other hand, the SSHI rectifier, when configured with inductances of 27, 56, and 120 μH, demonstrates significantly higher peak output powers of 124.9, 192, and 272.5 μW, respectively. This figure clearly illustrates the remarkable improvement in output power achieved by the SSHI rectifier compared to the FBR. Specifically, the SSHI rectifier with 120 μH inductance exhibits a 738% energy extraction enhancement compared to the FBR.

Table I compares the proposed DCB MPPT design and state-of-the-art MPPT techniques in energy harvesting systems. The previous works mainly focused on FOCV or P&O methods, while this work introduces the use of the duty cycle for MPPT. The DCB MPPT technique offers a simplified approach to achieve MPPT, as it is based on a straightforward equation and relies solely on the duty cycle of the rectifier. This translates into simpler circuit implementations, resulting in a compact chip area of only 0.47 mm^2. It has the ability to enable continuous MPPT without the need for power-hungry sensors. This further simplifies the overall system design and reduces complexity. Furthermore, the proposed DCB MPPT design offers the advantage of very low quiescent current consumption at only 0.17 μA. This low power requirement ensures minimal energy loss and maximizes the overall system efficiency. Another noteworthy aspect of the design is its independence from the system and environmental parameters, such as V_{OC} and η_F. This makes the DCB MPPT technique versatile and adaptable to different energy harvesting scenarios without the need for extensive parameter tuning. It boasts a flipping efficiency of 82% and 98% peak MPPT efficiency. Compared to an FBR, the DCB MPPT design offers a 738% power extraction enhancement.

VI. CONCLUSION

This article presents a novel DCB MPPT algorithm and its implementation with an SSHI rectifier. The duty cycle from the ac–dc rectifier is defined, and a simple equation between the MPPT efficiency and the duty cycle is derived. This shows that the MPPT efficiency solely depends on the duty cycle and remains unaffected by other system parameters. Building upon this equation, a bias-flip rectifier with the DCB MPPT technique is proposed in this article. The proposed method achieves MPPT by regulating the duty cycle, resulting in simplified circuit implementation. Experimental measurements validate the effectiveness and performance of this approach, showcasing a peak MPPT efficiency of 98% along with strong robustness and low power consumption. The applicability of the proposed DCB MPPT technique to other energy harvesting systems will be explored in future work.

ACKNOWLEDGMENT

The authors acknowledge Europractice for support in MPW and design tools, and Zu-Yao Chang from TU Delft for his valuable technical support.

REFERENCES

[1] Y. K. Ramadass and A. P. Chandrakasan, “An efficient piezoelectric energy harvesting interface circuit using a bias-flip rectifier and shared inductor,” *IEEE J. Solid-State Circuits*, vol. 45, no. 1, pp. 189–204, Jan. 2010.

[2] Z. Chen, M.-K. Law, P.-I. Mak, W.-H. Ki, and R. P. Martins, “Fully integrated inductor-less flipping-capacitor rectifier for piezoelectric energy harvesting,” *IEEE J. Solid-State Circuits*, vol. 52, no. 12, pp. 3168–3180, Dec. 2017.

[3] X. Yue and S. Du, “A synchronized switch harvesting rectifier with reusable storage capacitors for piezoelectric energy harvesting,” *IEEE J. Solid-State Circuits*, vol. 58, no. 9, pp. 2597–2606, Sep. 2023.

[4] S. Du, Y. Jia, C. Zhao, G. A. J. Amaratunga, and A. A. Seshia, “A fully integrated split-electrode SSHC rectifier for piezoelectric energy harvesting,” *IEEE J. Solid-State Circuits*, vol. 54, no. 6, pp. 1733–1743, Jun. 2019.

[5] D. A. Sanchez, J. Leicht, E. Jodka, E. Fazel, and Y. Manoli, “21.2 A 4μW-to-1 mW parallel-SSHI rectifier for piezoelectric energy harvesting of periodic and shock excitations with inductor sharing, cold start-up and up to 681% power extraction improvement,” in *IEEE Int. Solid-State Circuits Conf. (ISSCC) Dig. Tech. Papers*, Jan. 2016, pp. 366–367.

[6] X. Yue and S. Du, “Performance optimization of SSHC rectifiers for piezoelectric energy harvesting,” *IEEE Trans. Circuits Syst. II, Exp. Briefs*, vol. 70, no. 4, pp. 1560–1564, Apr. 2023.

[7] X. Yue, S. Javvaji, Z. Tang, K. A. A. Makinwa, and S. Du, “30.3 A bias-flip rectifier with a duty-cycle-based MPPT algorithm for piezoelectric energy harvesting with 98% peak MPPT efficiency and 738% energy-extraction enhancement,” in *IEEE Int. Solid-State Circuits Conf. (ISSCC) Dig. Tech. Papers*, Feb. 2023, pp. 442–444.

[8] A. Morel et al., “A shock-optimized SECE integrated circuit,” *IEEE J. Solid-State Circuits*, vol. 53, no. 12, pp. 3420–3433, Dec. 2018.

[9] X. Wang et al., “Multi-input SECE based on buck structure for piezoelectric energy harvesting,” *IEEE Trans. Power Electron.*, vol. 36, no. 4, pp. 3638–3642, Apr. 2021.

[10] P. Gasnier et al., “An autonomous piezoelectric energy harvesting IC based on a synchronous multi-shots technique,” in *Proc. ESSCIRC (ESSCIRC)*, Sep. 2013, pp. 399–402.

[11] S. Du and A. A. Seshia, “A fully integrated split-electrode synchronized-switch-harvesting-on-capacitors (SE-SSHC) rectifier for piezoelectric energy harvesting with between 358% and 821% power-extraction enhancement,” in *IEEE Int. Solid-State Circuits Conf. (ISSCC) Dig. Tech. Papers*, Feb. 2018, pp. 152–154.

[12] S. Javvaji, V. Singhal, V. Menezes, R. Chauhan, and S. Pavan, “Analysis and design of a multi-step bias-flip rectifier for piezoelectric energy harvesting,” *IEEE J. Solid-State Circuits*, vol. 54, no. 9, pp. 2590–2600, Sep. 2019.

[13] Y.-W. Jeong, S.-J. Lee, J.-H. Kim, M.-J. Cho, H.-S. Kim, and S.-U. Shin, “30.1 A scalable N-step equal split SSHI piezoelectric energy harvesting circuit achieving 1170% power extraction improvement and 22na quiescent current with a 1μH-to-10μH low Q inductor,” in *IEEE Int. Solid-State Circuits Conf. (ISSCC) Dig. Tech. Papers*, Feb. 2023, pp. 438–440.

[14] S. Li, A. Roy, and B. H. Calhoun, “A piezoelectric energy-harvesting system with parallel-SSHI rectifier and integrated MPPT achieving 417% energy-extraction improvement and 97% tracking efficiency,” in *Proc. Symp. VLSI Circuits*, Jun. 2019, pp. C324–C325.

[15] D. A. Sanchez, J. Leicht, F. Hagedorn, E. Jodka, E. Fazel, and Y. Manoli, “A parallel-SSHI rectifier for piezoelectric energy harvesting of periodic and shock excitations,” *IEEE J. Solid-State Circuits*, vol. 51, no. 12, pp. 2867–2879, Dec. 2016.

[16] S. Du, Y. Jia, C. D. Do, and A. A. Seshia, “An efficient SSHI interface with increased input range for piezoelectric energy harvesting under variable conditions,” *IEEE J. Solid-State Circuits*, vol. 51, no. 11, pp. 2729–2742, Nov. 2016.

[17] M. Shim, J. Kim, J. Jeong, S. Park, and C. Kim, “Self-powered 30 μW to 10 mW piezoelectric energy harvesting system with 9.09 ms/V maximum power point tracking time,” *IEEE J. Solid-State Circuits*, vol. 50, no. 10, pp. 2367–2379, Oct. 2015.

[18] Z. Chen, Y. Jiang, M.-K. Law, P.-I. Mak, X. Zeng, and R. P. Martins, “27.3 A piezoelectric energy-harvesting interface using split-phase flipping-capacitor rectifier and capacitor reuse multiple-VCR SC DC–DC achieving 9.3× energy-extraction improvement,” in *IEEE Int. Solid-State Circuits Conf. (ISSCC) Dig. Tech. Papers*, Feb. 2019, pp. 424–426.

[19] S. Uprety and H. Lee, “A 0.65-mW-to-1-W photovoltaic energy harvester with irradiance-aware auto-configurable hybrid MPPT achieving >95% MPPT efficiency and 2.9-ms FOCV transient time,” *IEEE J. Solid-State Circuits*, vol. 56, no. 6, pp. 1827–1836, Jun. 2021.

[20] A. Morel et al., “32.2 self-tunable phase-shifted SECE piezoelectric energy-harvesting IC with a 30nW MPPT achieving 446% energy-bandwidth improvement and 94% efficiency,” in *IEEE Int. Solid-State Circuits Conf. (ISSCC) Dig. Tech. Papers*, Feb. 2020, pp. 488–490.

[21] N. Femia, G. Petrone, G. Spagnuolo, and M. Vitelli, “Optimization of perturb and observe maximum power point tracking method,” *IEEE Trans. Power Electron.*, vol. 20, no. 4, pp. 963–973, Jul. 2005.

[22] S. Bandyopadhyay and A. P. Chandrakasan, “Platform architecture for solar, thermal, and vibration energy combining with MPPT and single inductor,” *IEEE J. Solid-State Circuits*, vol. 47, no. 9, pp. 2199–2215, Sep. 2012.

[23] S. Du, Y. Jia, C. Zhao, G. A. J. Amaratunga, and A. A. Seshia, “A passive design scheme to increase the rectified power of piezoelectric energy harvesters,” *IEEE Trans. Ind. Electron.*, vol. 65, no. 9, pp. 7095–7105, Sep. 2018.

[24] S. Li, X. Liu, and B. H. Calhoun, “A 32nA fully autonomous multi-input single-inductor multi-output energy-harvesting and power-management platform with 1.2×105 dynamic range, integrated MPPT, and multi-modal cold start-up,” in *IEEE Int. Solid-State Circuits Conf. (ISSCC) Dig. Tech. Papers*, vol. 65, Feb. 2022, pp. 1–3.

Xinling Yue (Graduated Student Member, IEEE) is currently pursuing the Ph.D. degree in microelectronics with the Electronic Instrumentation Laboratory, Delft University of Technology, Delft, The Netherlands.

She joined the Electronic Instrumentation Laboratory, Delft University of Technology, in December 2020. Her current research interests are energy-efficient power management integrated circuits and systems, which include energy harvesting, ac/dc rectifiers, dc/dc converters, and maximum power point tracking techniques.

Ms. Yue received the Best Student Paper Award at 2022 IEEE International Conference on Electronics Circuits and Systems (ICECS), Student Travel Grant Awards at 2022 IEEE International Symposium on Circuits and Systems (ISCAS) and 2023 International Solid-State Circuits Conference (ISSCC).

Sundeep Javvaji (Graduate Student Member, IEEE) received the B.Tech. degree from IIIT Nuzvid, Nuzvid, India, in 2015, and the M.S. degree from IIT Madras, Chennai, India, in 2018.

After that, he worked as an Analog Design Engineer at Texas Instruments, Bengaluru, India, till 2020. In December 2020, he joined as a Ph.D. Researcher at the Electronic Instrumentation Laboratory, Delft University of Technology (TU Delft), Delft, the Netherlands, where he is working on "low noise, high-speed ADCs."

Zhong Tang (Member, IEEE) received the B.S. and Ph.D. degrees in electrical engineering from Zhejiang University, Hangzhou, China, in 2015 and 2020, respectively.

From 2020 to 2023, he was a Post-Doctoral Researcher at the Electronic Instrumentation Laboratory, Delft University of Technology, Delft, The Netherlands. From 2019 to 2020, he was a Visiting Ph.D. Student with the EEIC Group, Eindhoven University of Technology, Eindhoven, The Netherlands. From 2016 to 2018, he was an Intern with Semitronix Corporation, Hangzhou, working on CMOS temperature sensor design. He is currently an Analog IC Designer with Vango Technologies Inc., Hangzhou, China. His research interests include CMOS temperature sensors and other precision analog and mixed-signal integrated circuits.

Kofi A. A. Makinwa (Fellow, IEEE) received the B.Sc. and M.Sc. degrees from Obafemi Awolowo University, Ife, Nigeria, in 1985 and 1988, respectively, the M.E.E. degree from the Philips International Institute, Eindhoven, The Netherlands, in 1989, and the Ph.D. degree from the Delft University of Technology, Delft, The Netherlands, in 2004.

From 1989 to 1999, he was a Research Scientist with Philips Research Laboratories, Eindhoven. Since 1999, he has been at the Delft University of Technology, where he is an Antoni van Leeuwenhoek Professor and the Head of the Microelectronics Department. His research interests include the design of mixed-signal circuits, sensor interfaces and smart sensors. This has led to 20+ books, 350+ technical articles, and 30+ patents.

Dr. Makinwa was a Distinguished Lecturer of the Solid-State Circuits Society and an Elected Member of its Adcom. He is a member of the Royal Netherlands Academy of Arts and Sciences. He is a co-recipient of 18 best paper awards, from the JSSC, ISSCC, and VLSI symposium, among others. At the 70th anniversary of ISSCC, he was recognized as its top contributor. He was the Analog Subcom Chair of ISSCC, and has served on the program committees of several other IEEE conferences. He is currently on the executive committee of the VLSI symposium and is a co-organizer of the Advances in Analog Circuit Design (AACD) workshop and the IEEE Sensor Interfaces Meeting (SIM).

Sijun Du (Senior Member, IEEE) received the B.Eng. degree (Hons.) in electrical engineering from University Pierre and Marie Curie (UPMC), Paris, France, in 2011, the M.Sc. degree (Hons.) in electrical and electronics engineering from the Imperial College, London, U.K., in 2012, and the Ph.D. degree in electrical engineering from the University of Cambridge, Cambridge, U.K., in January 2018.

He worked at the Laboratoire d'Informatique de Paris 6 (LIP6), University Pierre and Marie Curie, Paris, France, and then worked as a Digital IC Engineer in Shanghai, China, from 2012 to 2014. He was a Summer Engineer Intern at Qualcomm Technology Inc., San Diego, CA, USA, in 2016. He was a Visiting Scholar at the Department of Microelectronics, Fudan University, Shanghai, in 2018. He was a Post-Doctoral Researcher at the Berkeley Wireless Research Center (BWRC), Department of Electrical Engineering and Computer Sciences (EECS), University of California, Berkeley, CA, USA, from 2018 to 2020. In 2020, he joined the Department of Microelectronics, Delft University of Technology (TU Delft), Delft, The Netherlands, where he is currently an Assistant Professor. His current research is focused on energy-efficient integrated circuits and systems, including power management integrated circuits (PMIC), energy harvesting, wireless power transfer, and dc/dc converters used in Internet-of-Things (IoT) wireless sensors, wearable electronics, biomedical devices, and microrobots.

Dr. Du is a Technical Committee Member of the IEEE Power Electronics Society (PELS) and IEEE Circuits and Systems Society (CASS). He received the Dutch Research Council (NWO) Talent Program-VENI grant in the 2021 round. He was a co-recipient of the Best Student Paper Award from IEEE ICECS 2022. He served as a Sub-Committee Chair of IEEE ICECS 2022, a Review Committee Member of IEEE ISCAS from 2021 to 2023, and a Committee Member of the 2023 IEEE ISSCC Student Research Preview (SRP).